Energy & Environmental Science

PAPER

View Article Online
View Journal | View Issue

Cite this: *Energy Environ. Sci.*, 2015, **8**, 3646

A selectively exposed crystal facet-engineered TiO_2 thin film photoanode for the higher performance of the photoelectrochemical water splitting reaction†

Chang Woo Kim,‡[a] So Jin Yeob,‡[a] Hui-Ming Cheng[b] and Young Soo Kang*[a]

Received 24th July 2015,
Accepted 25th September 2015

DOI: 10.1039/c5ee02300a

www.rsc.org/ees

In the present study, a selectively exposed (101)-crystal facet engineered TiO_2 photoanode is investigated for the higher efficiency of the hydrogen evolution reaction. To date, even though the photoelectrochemical performance (PEC) dependent on exposed crystal facets has been calculated and demonstrated in semiconducting microcrystals, selectively exposed crystal facets of photocatalyst thin films have not been reported yet. Herein, we demonstrate a TiO_2 thin film photoanode with 100%-exclusively exposed crystal facets and suggest a methodology to obtain metal oxide thin film photoanodes with selectively exposed crystal facets. A selectively exposed crystal facet-manipulated metal oxide thin film photoanode is fabricated over pre-synthesized microcrystals through a three-step strategy: (1) hydrothermal synthesis of microcrystals, (2) positioning of microcrystals *via* polymer-induced manual assembly, and (3) fabrication of selectively exposed crystal facets of a TiO_2 thin film through a secondary growth hydrothermal reaction. Based on the synthesis of representative TiO_2 microcrystals with dominantly exposed (101), (100) and (001) crystal facets, the selectively exposed crystal faceted TiO_2 thin film photoanode is comparatively investigated for practical PEC performance. The photocurrent density of the selectively exposed (101) crystal faceted TiO_2 thin film photoanode is determined as 0.13 mA cm^{-2} and has an 18% conversion efficiency of incident photon-to-current at a 0.65 V Ag/AgCl potential under AM 1.5G illumination. Its photoelectrochemical hydrogen production reached 0.07 mmol cm^{-2} for 12 h, which is higher than those of (100) and (001) faceted photoelectrodes.

Broader context

The photoelectrochemical performance of a semiconducting photocatalyst for solar light fuel is related to solar light absorption, charge separation, charge transfer, and charge mobility, *etc.* Such considerations are attributed to the 3-dimensional atomic arrangement on the surface of the photocatalyst including coordination bonds between atoms and the presence/absence of dangling bonds. Tremendous efforts in facet engineering have been applied to various metal and metal oxide microcrystals. Even though some of the theoretical calculations and prediction of the surface energy of the crystal facet have been reported, there is a lack of study relating to proper comparison among thin films with different crystal facets because of the difficulty of fabricating thin films with exclusive one axis orientation and blocked or minimized other facet-exposure. We suggest a fabrication method for exclusively selected one crystal facet-exposed metal oxide thin films in three steps: the synthesis of microcrystals, monolayering of the microcrystals, and a second hydrothermal reaction.

Introduction

As an alternative energy to fossil fuels, solar energy is the most environmentally friendly and promising energy resource.[1–4] From an unlimited solar energy perspective, artificial photosynthesis has attracted significant attention for solar fuel production, such as hydrogen and C1 fuels. As this so-called artificial photosynthesis process, the photoelectrochemical (PEC) process is a suitable integrated energy conversion system for solar fuel production through water photoelectrolysis.[5,6]

[a] *Korea Center for Artificial Photosynthesis and Department of Chemistry, Sogang University, Seoul 121-742, Republic of Korea. E-mail: yskang@sogang.ac.kr*
[b] *Shenyang National Laboratory for Materials Science, Institute of Metal Research, Chinese Academy of Sciences, 72 Wenhua Rd, Shenyang 110016, China*

† Electronic supplementary information (ESI) available: Microscopic observation and XRD patterns of the microcrystals and UV-vis optical absorption diffuse reflectance curves. See DOI: 10.1039/c5ee02300a

‡ These authors contributed equally to the research.

Recent research has been devoted to solar light absorption efficiency, charge separation efficiency and surface charge transfer efficiency for integrated solar energy conversion.[7] In particular, the strategy for PEC enhancement has been focused on the manipulation of photo-reactive exposed crystal facet photocatalysts since the systematic demonstration of surface energy-dependent photocatalytic PEC performance by the Cheng group and Lee group.[3,8] They reported the dramatic impact of PEC performance in anatase TiO_2 microcrystals with a dominantly exposed (001) facet. Furthermore, {001}, {010}, and {101}-dominantly faceted TiO_2 microcrystals have been manipulated with F^- ions.[9] As for the crystal facet-dependent properties of photocatalysts, the PEC performance of metal oxide microcrystals of photocatalysts such as facet-selective ZnO nanorods,[10,11] {002}, {200} and {020} facet engineered WO_3 quasi-cubic crystals,[12] polyhedral Cu_2O microcrystasl,[13] $BiVO_4$ microcrystals with dominant (040) facet[14] and BiOCl nanosheets with {001} facet[15,16] have been reported recently and suggested for the higher efficiency of the water splitting reaction. The atomic arrangement at the crystal surface of the selected crystal facet of the photocatalyst provides a specific photo-activity and reactive site. Such an atomic arrangement at the surface leads to a specifically exposed crystal facet to show the enhancement of PEC performance.

Even the surface energy calculated from the atomic arrangement would be effective for enhanced PEC performance, this enhancement has been demonstrated by photocatalysts with selectively exposed dominant crystal facets.[17,18] Interestingly it would be controversial if the surface energy calculations dependent on the selectively exposed crystal facets of a photocatalyst microcrystal did not match with the PEC performance of the microcrystals.[9,19] In particular, to better understand the PEC performance of each crystal facet, microcrystals/2 dimensional (2D) thin film of photocatalysts with a selectively exposed crystal facet would be required. However, a directly grown TiO_2 thin film with a dominant crystal facet selectively exposed from the substrate has not been reported with hydrothermal/solvothermal methods.[20,21] It is difficult to prepare photocatalyst microcrystal thin films that could expose a single facet selectively, and, further, suitable methodology for proving the real PEC performance of the selected single crystal facet is rare. Single crystal facet-exposed thin films have usually been fabricated by deposition methods such as chemical vapor deposition and atomic layer deposition.[22] However, these deposition techniques are typically expensive, slow, provide a limited choice of active materials and are not available for large surface areas.[23] In addition, they cannot modulate the facet selectivity of the photocatalysts and could not be expected to improve PEC performance from facet engineering.

In the present study, we demonstrate a selectively exposed crystal facet-engineered TiO_2 thin film photoanode. Based on our previous research about the synthesis of microcrystals[24] and second-hydrothermal reactions,[20,25,26] we suggest a methodology to produce a metal oxide photoanode with a selectively exposed crystal facet. A selectively exposed crystal faceted TiO_2 thin film photoanode has been comparatively studied for practical PEC performance in hydrogen evolution between the TiO_2 photoanode with selectively exposed (101), (100), and (001) crystal facets. This suggested methodology is the first to demonstrate the scientific significance of PEC performance dependent on the selectively exposed crystal facets of a TiO_2 thin film. We hope that the results of this study contribute to the design of efficient metal oxide photoanodes for enhanced solar fuel production.

Experimental

Materials

Titanium oxysulfate–sulfuric acid complex hydrate ($TiOSO_4 \cdot xH_2SO_4 \cdot xH_2O$, FW: 276 g mol^{-1}, Sigma-Aldrich, synthesis grade), titanium (powder, −100 mesh, 99.7% metal basis), hydrogen fluoride (48–50% of HF, J. T. Baker), polyethyleneimine (PEI) and ethyl alcohol were used without any further purification. Distilled water was used with a Milli-Q gradient included Quantum EX Cartridge Filter from EMD Millipore. F-doped tin oxide (FTO) coated glass (2 cm × 2 cm) obtained from Pilkington (Toledo, OH) was employed as a transparent conducting oxide.

Synthesis of dominantly (101) facet-exposed TiO_2 microcrystals (TO_{101})

TO_{101} bi-pyramidal microcrystals were synthesized by adding Ti powder (0.006 g), hydrogen peroxide (3 mL), HF (0.064 mL, 48–50%, 53 mM) and D.W. (27 mL) into a microwave reaction vessel. The prepared mixture was continuously stirred for 3 h until a clear yellow solution was obtained. The microwave hydrothermal treatment was carried out in a MARS (0–1200 watts ± 15%, 2450 MHz, CEM Corporation). The temperature and pressure were controlled with a RTP-300 Plus and a ESP-1500 Plus sensor, respectively. The reaction was performed at 180 °C for 4 h. After the reaction was complete, the reactor was cooled with flowing water and the white powder product was collected by centrifugation, washed several times and dried. For the synthesis of the dominantly (100) facet-exposed TiO_2 (TO_{100}, rectangular-shape) and dominantly (001) facet-exposed TiO_2 (TO_{001}, plate-shape) microcrystals, 45 mM and 85 mM aqueous HF solutions were used in the reactions. Titanium oxysulfate–sulfuric acid complex hydrate (100 mg) was dissolved in each prepared 45 mM and 85 mM aqueous HF solution (133 mL) and stirred for 2 h until the suspensions became transparent. The resultant solutions were transferred to Teflon lined autoclaves and heated at 180 °C for 2 h (TO_{100}) and 12 h (TO_{001}), respectively. After the reaction was complete, the same procedure was applied as described above. The as-prepared white resultants (TO_{101}, TO_{100} and TO_{001}) were heated at 600 °C under air in a furnace for 2 h.

Fabrication of secondary reacted thin film photoanodes (sTO_{101}, sTO_{100} and sTO_{001})

A clean FTO was spin-coated with 2.0 wt% PEI at a speed at 2000 rpm for 20 s. The as-synthesized TiO_2 microcrystals (TO_{101}, TO_{100} and TO_{001}) were placed and assembled on the PEI-coated substrates. The as-prepared monolayer films (mTO_{101}, mTO_{100} and mTO_{001}) were heat-treated at 500 °C for 3 h to remove the

polymeric PEI linker. For a typical synthesis of sTO_{100}, mTO_{100} was placed in a similar solution as previously used to prepare TO_{100} for 2 h. mTO_{100} was then transferred to an oven and heated at 200 °C for 2 h. mTO_{101} and mTO_{001} were placed in a solution containing 35 wt% HCl (0.018 mL), TiF_4 (0.10 g), NaCl (0.935 g) and D.W. (20 mL) and secondly reacted at 200 °C for 1.5 h and 4 h, respectively, for the sTO_{101} and sTO_{001} photoanodes. Each of the secondary growth TiO_2 films (sTO_{101}, sTO_{100}, sTO_{001}) was annealed at 500 °C for 3 h.

Characterization

Crystallographic information for all the samples was obtained by X-ray diffraction (XRD) (Rigaku miniFlex-II desktop X-ray diffractometer, Cu Kα radiation with λ = 0.154056 nm). Microscopic observation of all the samples was carried out with field emission scanning electron microscopy (Hitachi S-4300 FE-SEM). Transmission electron microscope (TEM) images and selected area (electron) diffraction (SAED) patterns were obtained with a JEOL transmission electron microscope (JEM 2100F) at a 200 keV accelerating voltage. The optical properties including the band energies of all the samples were monitored and determined from diffuse reflectance spectra (DRS) using a Varian Cary 5000 UV-Vis-NIR Spectrophotometer (Agilent Technologies) and FTO glass was used as the reference to characterize the absorbance.

Photoelectrochemical measurements

Photoelectrochemical measurements of the photoanodes as working electrode were conducted with a PL-9 potentiostat in a conventional three-electrode system. A 300 W Xe arc lamp was used to simulate solar illumination through an AM 1.5G filter (Asahi HAL-320, 100 mW cm^{-2}). Before PEC measurement, the power density of the incident light was adjusted to 100 mW cm^{-2} using a NREL certified reference cell (Photo Emission Tech., Inc.). The illumination was set as a back-side illumination to the FTO surface. The illuminated area was a circle of area 0.38 cm^2 (0.7 cm of diameter) at room temperature under 1 sun illumination. Having employed a Pt electrode and an Ag/AgCl reference electrode in aqueous Na_2SO_4 solution (0.5 M, pH = 6.8), the *I–V* curve was plotted at a scan rate of 20 mV s^{-1} with scanning of the potential in the positive direction. An *I–t* curve was observed under constant bias. All the PEC measurements were done using an Ag/AgCl (2.0 M of KCl) reference electrode. Electrochemical impedance spectroscopy (EIS) curves were obtained from 0.1 to 105 Hz and recorded at 0.65 V *vs.* Ag/AgCl. The incident photon to current conversion efficiency (IPCE) was determined from 300 to 800 nm with an applied potential of 0.65 V.

Hydrogen gas production measurements

Hydrogen gas evolution experiments were carried out in an air-tight continuous flow cell connected with the online GC system (Agilent 7890A) equipped with a pulsed discharge detector (PDD). Each 30 mL PEC cell had Nafion 117 proton transfer material between the photoanode and Pt counter electrode. 1.13 cm^2 of the illuminated areas of the photoanode and Pt counter electrode was separately applied to 15 mL of 0.5 M Na_2SO_4 aqueous solution with Ag/AgCl as the reference electrode. After flushing with He gas (99.9999%) at a flow rate of 10 mL min^{-1} for 3 h to remove air under dark conditions, the working electrode was illuminated with a continuous flow of He (10 mL min^{-1}). The evolved gas was checked every hour for 12 h at 0.65 V (*vs.* Ag/AgCl) with 1500 rpm of stirring at room temperature under 1 sun irradiation (Asahi HAL-320, 100 mW cm^{-2}). The complete water splitting reaction requires a total potential of 1.23 eV (RHE) which is equivalent to 0.65 V (*vs.* Ag/AgCl, ESI†).

Electrical conductivity measurements

Electrical conductivity measurements, dependent on the facets of TiO_2 microcrystals, were carried out by obtaining *I–V* curves with a probe station, which was installed in the Shenyang National Laboratory for Materials Science (Prof. H.-M. Cheng, Institute of Metal Research, China). One drop of the TiO_2 microcrystals in ethanol was placed on a silicon substrate and dried. The substrate was loaded into a field emission scanning electron microscope (FE-SEM, NOVA NANOSEM 430) with two picoprobe tungsten tips (PT-14-6705-13), which were set into the arms with a Kleindiek Nanotechnik controller. For measuring the *I–V* curves, a Keithley semiconductor characterization system (4200-SCS) was connected to the two tungsten tips. The current was measured with a potential range of −0.5 to 5.0 V.

Experimental details for fluorescence lifetime measurements

Fluorescence lifetime decays were measured using an inverted-type scanning confocal microscope (MicroTime-200, Picoquant, Germany) with a 20× objective. The measurements were performed at the Korea Basic Science Institute (KBSI), Daegu Center, South Korea. A single-mode pulsed diode laser (375 nm with an instrumental response function of ~240 ps in pulse width, a repetition rate of 5 MHz, and a laser power of ~5 μW) was used as an excitation source. A dichroic mirror (Z375RDC, AHF), a longpass filter (HQ405lp, AHF), and an avalanche photodiode detector (PDM series, MPD) were used to collect entire emission from the film samples. Time-resolved fluorescence photon counting and exponential fitting of the obtained fluorescence decays were performed using SymPhoTime software (version 5.3).

Results and discussion

For the 100% selectively exposed-(101) facet of the TiO_2 microcrystal (TO_{101}), a bi-pyramidal TiO_2 microcrystal was newly designed and prepared with H_2O_2 and HF. For comparison of crystal facet-dependent photochemical properties, TiO_2 microcrystals with dominantly exposed (100) and (001) facets (TO_{100} and TO_{001}) were synthesized by controlling the atomic ratio of Ti/F in the precursor solutions.[27] Microscopic observation of each TiO_2 microcrystal was achieved *via* high resolution transmission electron microscopy (HRTEM) and selected area electron diffraction (SAED) as shown in Fig. 1. TO_{101} was a bi-pyramidal shaped microcrystal with 300 nm × 300 nm dimensions. The scanning electron microscopic (SEM) image in Fig. S1 (ESI†) indicated that all exposed facets were 8-(101) facets.

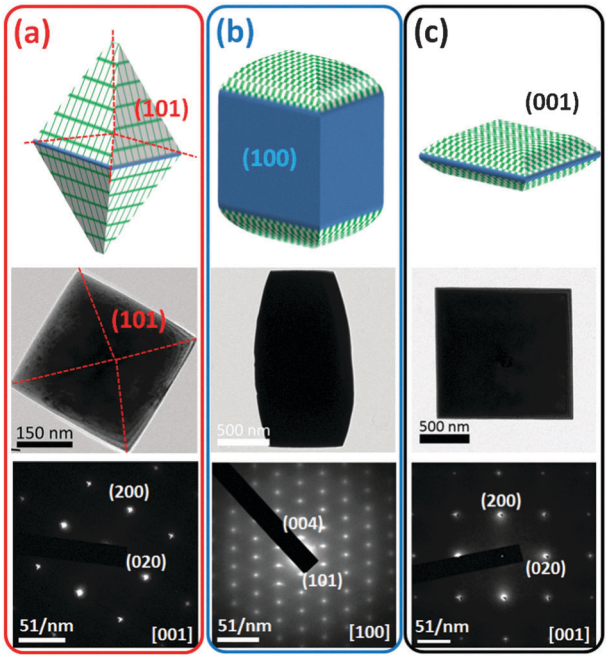

Fig. 1 Scheme, typical TEM images and SAED patterns of bi-pyramidal TO_{101} (a), cuboid TO_{100} (b) and plate TO_{001} (c) microcrystals.

TO_{100} was determined to be a cuboid-shaped microcrystal with 1.1 μm × 1.5 μm dimensions. It was shown to have up/downward 2-(001) facets surrounding lateral 4-(100) facets. TO_{001} was a plate-shaped microcrystal with 1.5 μm × 1.5 μm dimensions, exposing dominantly up/downward 2-(001) facets. The microscopic observations are shown in Fig. 1 and Fig. S2 (ESI†), and matched with crystallographic information from X-ray powder diffraction (XRD) in Fig. S3 (ESI†). This indicates that the lattice fringes of TO_{101}, TO_{100}, TO_{001} with *d* spacing values of 0.133, 0.237, and 0.189 nm correspond to the (220), (004), and (200) facets, respectively. All the samples, TO_{101}, TO_{100}, TO_{001} are determined to be single crystalline microcrystals and each TiO_2 microcrystal appears to be dominantly exposed with the selected (101), (100) and (001) crystal facet, respectively.

Each TO microcrystal with each dominantly exposed crystal facet was introduced to a one-axis oriented TiO_2 monolayer (mTO) photoanode to study the facet dependent PEC performance. A one-axis oriented monolayer of each TO microcrystal was fabricated by a polyethyleneimine (PEI)-induced manual assembly technique, which can be used to prepare a 2D monolayer with exposed crystal facets.[24–26] The selectively exposed crystal facet-manipulated TiO_2 thin film photoanode is fabricated through a three-step strategy in Fig. 2. The pre-synthesized TiO_2 microcrystals with each dominant crystal facet were positioned on the FTO with a PEI-induced manual assembly, in which the imine group of the PEI formed a covalent bond with oxygen on the FTO surface.[28,29] This resulted in the formation of a monolayer of TiO_2 microcrystals on the substrate surface. Each TO microcrystal is aligned and its dominantly exposed facet faces upward. After that, a secondary growth hydrothermal reaction drives upward-growth from the substrate. Voids among

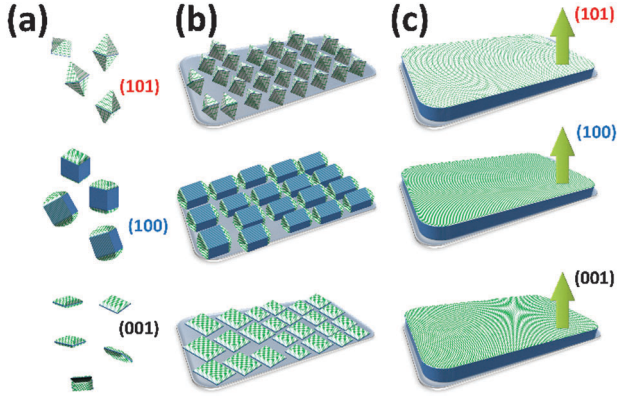

Fig. 2 Scheme of upward-facet exposed metal oxide photoanode. Metal oxide microcrystals (a) were assembled to monolayer-films (b) and upward-faceted films (c) were fabricated *via* a second-hydrothermal reaction.

the TiO_2 microcrystals were filled and the other facets were covered, finally resulting in TiO_2 thin films with selective upward-targeted crystal facet exposure. As shown in Fig. 2, each TO microcrystal was assembled to form a monolayer thin film by PEI-induced manual assembly on FTO glass. Fig. 2(b) shows schematic illustrations of the monolayered TO_{101} film (mTO_{101}), monolayered TO_{100} film (mTO_{100}) and monolayered TO_{001} film (mTO_{001}) after PEI-induced manual assembly. Fig. 2(c) shows schematic illustrations of the secondary growth TO_{101} film (sTO_{101}), TO_{100} film (sTO_{100}) and TO_{001} film (sTO_{001}).

In Fig. 3 and Fig. S4 (ESI†), typical SEM images show that the voids and gaps among the microcrystals were filled and lateral facets were covered by the secondary growth hydrothermal reaction. With each exposed crystal facet, the *c*-axis of the sTO was matched with the most intense XRD peak. mTO_{101} with exposed 7-(101) facets was vertically aligned to [101] as a *c*-axis. This resulted in the most intense peak corresponding to (101) at 25° from the XRD pattern with the other peaks from the

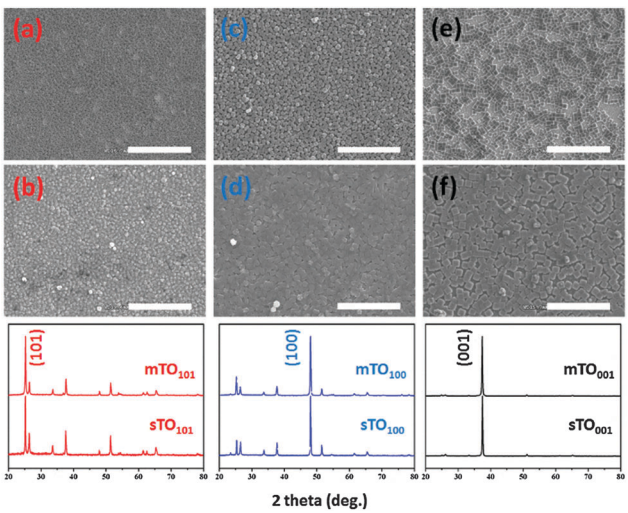

Fig. 3 Typical SEM images and XRD patterns of mTO_{101} (a), sTO_{101} (b), mTO_{100} (c), sTO_{100} (d), mTO_{001} (e) and sTO_{001} (f) (scale bar in SEM images; 20 μm).

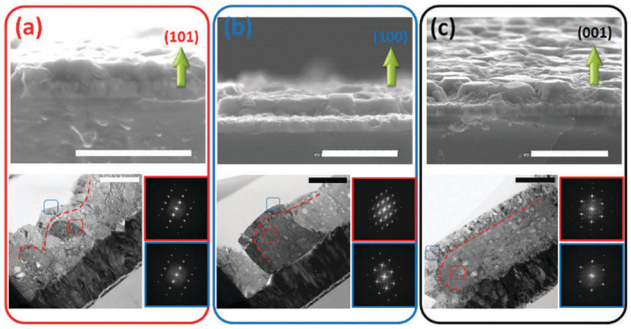

Fig. 4 Typical cross-sectional SEM (scale bar: 5 μm), TEM images (scale bar: 0.2 μm) and FFT images (red square: former crystal; blue square: latter crystal) of sTO_{101} (a), sTO_{100} (b) and sTO_{001} (c).

FTO substrate. Likewise, the 4-(100) and 2-(001) facet-exposed mTO_{100} and dominant 2-(001) facet-exposed mTO_{001} were vertically aligned to [100] and [001] as *c*-axes and this resulted in (100) and (001) at 48° and 37.5°, respectively, from the XRD spectra. Interestingly, after the other crystal facets in mTO were covered in the secondary growth hydrothermal reaction, the upward facets of the mTOs, such as (101) in mTO_{101}, (100) in mTO_{100} and (001) in mTO_{001}, stayed upwardly exposed. SEM and XRD of sTO clearly indicate that the (101) facet in sTO_{101}, the (100) facet in sTO_{100} and the (001) facet in sTO_{001} stayed as upwardly exposed facets and their perpendicular orientation was also maintained as the *c*-axes shown in Fig. 4.

Cross-sectional TEM images using a focused ion beam (FIB) showed that the upward facing crystal facet in each sTO had a growth direction along the *c*-axis after the secondary growth hydrothermal reaction. It is worth noting that the crystal phase formed by the secondary growth was distinguishable from the pre-existing single crystal phase (mTO) and it was single crystalline with the same growth direction as that shown in the cross sectional TEM images and fast Fourier transform (FFT) images. SEM images of the mTO and sTO films in Fig. S5 and S6 (ESI†) indicate that the film thickness of sTO_{101} was determined as 0.937 μm from 0.781 μm of mTO_{101}. The thicknesses of sTO_{100} (0.984 μm) and sTO_{001} (1.015 μm) were also increased from mTO_{100} (0.765 μm) and mTO_{001} (0.796 μm). Thus, our microscopic and crystallographic observations support the idea that a TiO_2 thin film photoanode with an exclusively exposed crystal facet on the FTO substrate was successfully fabricated.

The PEI-induced manual assembly technique arranges a selective crystal facet-exposed TiO_2 particle monolayer film spontaneously on a substrate to make a one-axis oriented monolayer. In addition, it also allows the comparative study of the real efficiency of one-axis oriented TiO_2 thin films with selectively exposed single crystal facets in actual PEC systems. Fig. 5 shows that the photocurrent densities of sTO_{101}, sTO_{100} and sTO_{001} at 0.65 V were determined to be 0.13, 0.07, and 0.02 mA cm^{-2}, respectively. Even though all TiO_2 thin film photoanodes had a −0.5 V (*vs.* Ag/AgCl) onset potential (V_{op}), such a tendency of the photocurrent density from each facet was matched with the order of the incident photon to electron conversion efficiency (IPCE) values of each TiO_2 thin film

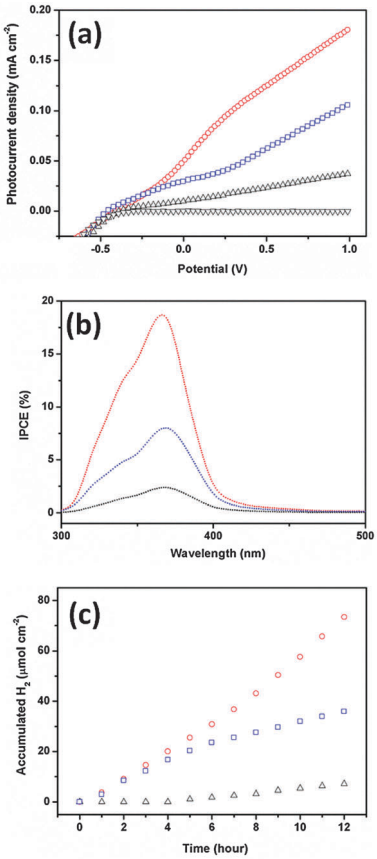

Fig. 5 *I–V* curve (a), IPCE (b) and gas evolution rate (c) of sTO_{101} (red), sTO_{100} (blue) and sTO_{001} (black).

photoanode. All sTO were revealed to have a 367 nm λ_{max} and a 460 nm onset wavelength (λ_{op}). sTO_{101} produced the highest IPCE value of 18%, compared with 8% for sTO_{100} and 2% for sTO_{001} at a 367 nm λ_{max}. The hydrogen evolution efficiency was also investigated for sTO_{101}, sTO_{100}, and sTO_{001} based on the facet dependent *I–V* and IPCE results. Under conditions of hydrogen gas evolution, in Fig. 5(c), Fig. S7 and S8 (ESI†) show the hydrogen gas evolution rate for the sTO photoanode under AM 1.5G. It is worth noting that sTO_{101} evolved the largest amount of hydrogen gas, 73 μmol cm^{-2}, compared with 36 μmol cm^{-2} for sTO_{100} and 7 μmol cm^{-2} for sTO_{001} over 12 h. Under UV irradiation, the hydrogen gas evolution of sTO_{101} reached 1.0 mmol cm^{-2} and sTO_{100} and sTO_{001} produced 0.8 mmol cm^{-2} and 0.3 mmol cm^{-2}, respectively, as shown in Fig. S9 (ESI†). The solar-to-hydrogen conversion efficiency (ηSTH) was measured in a 3-electrode system using the following equation, assuming a faradaic efficiency of 100% when considering applied potential.[30] ηSTH is beneficial in describing the whole of the PEC process for water splitting. Interestingly, the ηSTH of sTO_{101} was calculated to be 0.077% at 0.65 V. This enhancement in ηSTH for sTO_{101} comes from along the (101)-axis, in which the crystal facet dependent PEC performance was comparable with the value of 0.053% in the previous report.[30] Typical ηSTH values of sTO_{100} and sTO_{001} were determined as 0.040% and 0.012%, respectively.

Strikingly, these results are not consistent with those predicted by computational calculation on the surface energy of each facet of TiO_2 microcrystal. Theoretically PEC performance has been demonstrated to have an ordering of (001) > (100) > (101), based on the surface energy of the anatase TiO_2 microcrystal.[31] Although dominant exposure of crystal facets in TiO_2 microcrystals was compared and the surface energy of the (001) facet is thermodynamically the highest, our observation apparently indicates that sTO_{101} coherently produced the highest PEC performance. For a better understanding of the PEC ordering, $sTO_{101} > sTO_{100} > sTO_{001}$, each TiO_2 thin film photoanode was studied from the aspects of light harvesting, electrical conductivity and interfacial impedance. The light harvesting ability of each TiO_2 thin film photoanode was investigated by determining the optical absorption coefficient, shown in Fig. S10 (ESI†). The optical absorption coefficient decreased from 16.7 nm^{-1} for sTO_{101} to 13.4 nm^{-1} and 16.6 nm^{-1} for sTO_{100} and sTO_{001}, respectively. Additionally, the electrical conductivity was investigated using the facets of the TO microcrystals by contacting the selected crystal facets with a probe station with tungsten tips.[32] Images of the surface current measurements using the probe station are shown in the inset of Fig. 6. The electrical conductivity along the *c*-axis of the TO microcrystals with different crystal facets was determined to be between −5.0 and 5.0 V. The electrical connection between the (001) facets in the TO_{001} microcrystals produced a surface current of *ca.* 10 μA. Even the surface current between the (001) and (101) facets in the TO_{001} microcrystals was *ca.* 30 μA. The highest current was observed to be *ca.* 50 μA in the electrical connection between the (101) facets. The results show that electrical conductivity caused by electrical connection between two (101) facets of TO microcrystal was the highest. Electrical connection was more favorable between (101) facets than the others.

Together with facet dependent-optical and electrical properties, the interfacial impedance between the surface of the TiO_2 thin film with each crystal facet and electrolyte solution was measured for interfacial charge transfer through the interface, this is shown in Fig. 7 which shows a comparison of Nyquist

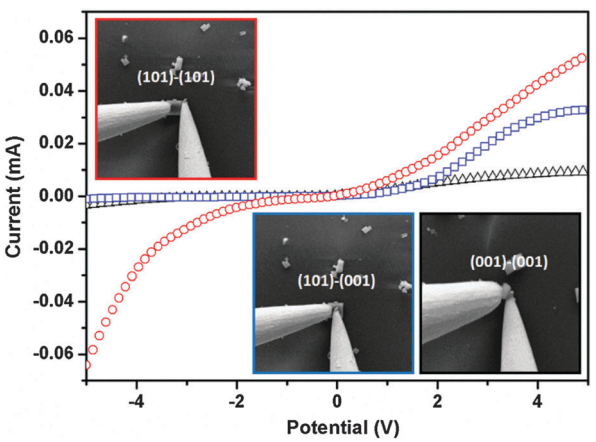

Fig. 6 Facet-dependent electrical conductivity between (101) and (101) in sTO_{101} (red), (101) and (001) (blue), and (001)–(001) in sTO_{001} (black).

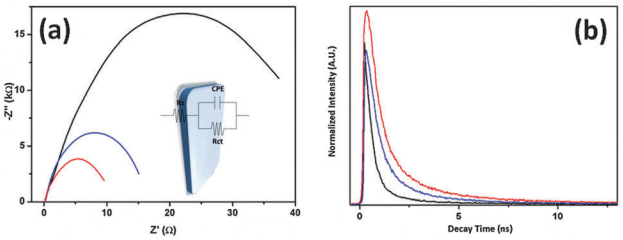

Fig. 7 Nyquist plot (a) and time resolved photoluminescence (b) for sTO_{101} (red), sTO_{100} (blue) and sTO_{001} (black).

plots among the sTO photoanodes. Electrical impedance spectroscopy (EIS) experiments were used to determine the charge transfer resistance (R_{ct}) at the interface between the surface of the TiO_2 thin film photoanodes with each crystal facet and the electrolyte solution under solar light illumination. In the Nyquist plots of the sTO thin film photoanodes, the presence of semicircles is related to the charge-transfer resistance at the counter electrode, electron transport at the interface of the photoelectrode/electrolyte solution and mass transport in electrolyte.[33] In particular, the secondary arc of the Nyquist plots is attributed to the interfacial charge transfer kinetics. Since the semicircle is derived from the recombination resistance at the interface between the surface of the TiO_2 thin film photoanode with each crystal facet and electrolyte solution, the resistance value increases in the following order: $sTO_{101} < sTO_{100} < sTO_{001}$. Among them, sTO_{101} exhibits the highest photovoltaic performance, owing to its low interfacial impedance for charge transfer.[33] This enhanced PEC performance of the kinetics of the photogenerated charge carriers was confirmed with time-resolved photoluminescence (TRPL) at room temperature in Fig. 7(b). From the excitation wavelength at 375 nm, transient emission was observed in sTO_{101} (red), sTO_{100} (blue) and sTO_{001} (black), respectively. The average decay time (τ_{ave}) of the charge carriers in sTO_{101} was 20.832 ns which is longest τ_{ave} compared with 11.319 ns and 10.337 ns in sTO_{100} and sTO_{001}, respectively. τ_{ave} of the charge carriers in sTO_{101} is significantly increased compared with those in sTO_{100} and sTO_{001}, which indicates that the (101)-crystal facet in sTO_{101} enhances the charge separation efficiency and retards charge recombination at the interfacial solid–liquid junction.

The impedance at the interface between the TiO_2 thin film photoanode and electrolyte solution was the lowest for sTO_{101}. The order of the interface impedance values of the sTO reveals that the higher photoreactive properties of sTO_{101} are related to its higher faradaic current. In addition, the diffusivity of the photo-generated electrons in the TiO_2 thin film photoanode could be proved with the electron mobility along the *c*-axis, *i.e.* the (101)-, (100)-, and (001)-axis, because electrons are transported along the *c*-axis of the TiO_2 thin film photoanodes to reach the transparent conducting substrate to determine the photocurrent density of the considered photoanode. Electron diffusion along the *c*-axis of the TiO_2 thin film photoanode can be controlled by the bond lengths between Ti and O in the three-dimensional crystal structure of the regular repeating layers of TiO_2.[34] The three dimensional crystal structures of

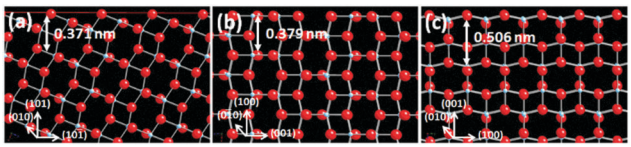

Fig. 8 Three-dimensional atomic arrangement of anatase TiO_2 microcrystals along the (101), (100), and (001) facets. The surface crystal structure of each facet controlled TiO_2 was simulated by crystal maker™ software based on the structure of anatase TiO_2 (a = 3.785, b = 3.785, c = 9.5140, and $\alpha = \beta = \gamma = 90°$).

the anatase TiO_2 microcrystals along the (101), (100), and (001) facets are shown in Fig. 8. A short bond length of the regular atomic arrangement in the crystal structures of the TiO_2 particles allows faster electron diffusivity along the *c*-axis. In Fig. 8, the distance between layers along the (101)-axis was the shortest (0.371 nm). Thus, electrons can diffuse along the (101)-axis faster than the other axes. The lengths between layers along the (100)- and (001)-axis were calculated as 0.379 and 0.506 nm, respectively. In addition to electrical conductivity, interfacial resistance and diffusivity of charge along the *c*-axis are also critical parameters for the PEC performance of each crystal facet. An extraordinarily high PEC performance of the TiO_2 thin film photoanode with the (101) facet was attributed to the electrical conductivity, interfacial resistance and diffusivity of charge along the *c*-axis.

Conclusions

In summary, we demonstrated that a TiO_2 thin film photoanode with a selectively exposed crystal facet was better for the higher performance of efficient hydrogen gas evolution. Each facet-exposed TiO_2 thin film photoanode was fabricated using TiO_2 microcrystals with exclusive dominant exposure of each of the (101), (100), and (001) facets by a PEI induced manual assembly technique and a secondary growth hydrothermal reaction. Fabrication of each selectively exposed (101), (100), and (001) crystal facet TiO_2 thin film photoanode, which have different *c*-axis arrangements, was carried out to study the comparative PEC performance of each crystal facet. We observed higher PEC performance of the TiO_2 thin film photoanode with a selectively exposed (101) crystal facet than those of the (100) and (001) facets. We investigated the reason that the selectively exposed (101) crystal facet produced a higher improvement from the aspects of electrical conductivity, interfacial resistance and diffusivity of charge along the *c*-axis. Along with the photocurrent density trend, similar trends in the optical absorption coefficient, electron diffusivity, IPCE, and the energy barrier at the interface of TiO_2 thin film photoanode/electrolyte solution further supported the water splitting reaction efficiency of each different crystal facet TiO_2 thin film photoanode. sTO_{101} evolved the largest amount of hydrogen gas, which could be attributed to the largest photon absorption capacity of the (101) crystal surface, the highest electron diffusivity along the *c*-axis, the highest IPCE, and the lowest resistance at the interface of sTO_{101}/electrolyte solution.

Acknowledgements

Artificial Photosynthesis (KCAP) located in Sogang University (No. 2009-0093885) funded by the Minister of Science, ICT and Future Planning (MSIP) through the National Research Foundation of Korea and the Brain Korea 21 Plus Project 2015. The authors thank Dr Weon-Sik Chae, KBSI Daegu Center, for the fluorescence lifetime measurements.

Notes and references

1 D. Kim, K. K. Sakimoto, D. Hong and P. Yang, *Angew. Chem., Int. Ed.*, 2015, **54**, 3259–3266.
2 M. G. Walter, E. L. Warren, J. R. McKone, S. W. Boettcher, Q. Mi, E. A. Santori and N. S. Lewis, *Chem. Rev.*, 2010, **110**, 6446–6473.
3 Y. Ma, X. Wang, Y. Jia, X. Chen, H. Han and C. Li, *Chem. Rev.*, 2014, **114**, 9987–10043.
4 Y. Tachibana, N. Vayssieres and J. R. Durrant, *Nat. Photonics*, 2012, **6**, 511–518.
5 J. Barber, *Chem. Soc. Rev.*, 2009, **38**, 185–196.
6 N. S. Lewis and D. G. Nocera, *Proc. Natl. Acad. Sci. U. S. A.*, 2006, **103**, 15729–15735.
7 Z. Chen, H. Dinh and E. Miller, *Photoelectrochemical Water Splitting: Standards, Experimental Methods, and Protocols*, Springer, 2013.
8 G. Liu, H. G. Yang, J. Pan, Y. Q. Yang, G. Q. (Max) Lu and H.-M. Cheng, *Chem. Rev.*, 2014, **114**, 9559–9612.
9 J. Pan, G. Liu, G. Q. (Max) Lu and H.-M. Cheng, *Angew. Chem., Int. Ed.*, 2011, **50**, 2133–2137.
10 F.-R. Fan, Y. Ding, D.-Y. Liu, Z.-Q. Tian and Z. L. Wang, *J. Am. Chem. Soc.*, 2009, **131**, 12036–12037.
11 J. Joo, B. Y. Chow, M. Prakash and E. S. Boyden, *Nat. Mater.*, 2011, **10**, 596–601.
12 Y. P. Xie, G. Liu, L. Yin and H.-M. Cheng, *J. Mater. Chem.*, 2012, **22**, 6746–6751.
13 S. Sun, X. Song, Y. Sun, D. Deng and Z. Yang, *Catal. Sci. Technol.*, 2012, **2**, 925–930.
14 D. Wang, H. Jiang, X. Zong, Q. Xu, Y. Ma, G. Li and C. Li, *Chem. – Eur. J.*, 2011, **17**, 1275–1282.
15 D.-H. Wang, G.-Q. Gao, Y.-W. Zhang, L.-S. Zhou, A.-W. Xu and W. Chen, *Nanoscale*, 2012, **4**, 7780–7785.
16 H. Cheng, B. Huang and Y. Dai, *Nanoscale*, 2014, **6**, 2009–2026.
17 W.-N. Zhao and Z.-P. Liu, *Chem. Sci.*, 2014, **5**, 2256–2264.
18 J. Yang, D. Wang, X. Zhuo and C. Li, *Chem. – Eur. J.*, 2013, **19**, 1320–1326.
19 H. G. Yang, C. H. Sun, S. Z. Qiao, J. Zou, G. Liu, S. C. Smith, H.-M. Cheng and G. Q. Lu, *Nature*, 2008, **453**, 638–641.
20 T. K. Van, C. K. Nguyen and Y. S. Kang, *Chem. – Eur. J.*, 2013, **19**, 9376–9380.
21 B. Liu and E. S. Aydil, *Chem. Commun.*, 2011, **47**, 9507–9509.
22 D. A. Boyd, L. Greengard, M. Brongersma, M. Y. El-Naggar and D. G. Goodwin, *Nano Lett.*, 2006, **6**, 2592–2597.
23 J. Liu, H. G. Zhang, J. Wang, J. Cho, J. H. Pikul, E. S. Epstein, X. Huang, J. Liu, W. P. King and P. V. Braun, *Adv. Mater.*, 2014, **26**, 7096–7101.

24 C. W. Kim, Y. S. Son, A. U. Pawar, M. J. Kang, J. Y. Zheng, V. Sharma, P. Mohanty and Y. S. Kang, *J. Mater. Chem. A*, 2014, **2**, 6057–6066.
25 H. G. Cha, M. J. Kang, I. C. Hwang, H. Kim, K. B. Yoon and Y. S. Kang, *Chem. Commun.*, 2015, **51**, 6407–6410.
26 J. Y. Zheng, G. Song, J. Hong, T. K. Van, A. U. Pawar, D. Y. Kim, C. W. Kim, Z. Haider and Y. S. Kang, *Cryst. Growth Des.*, 2014, **14**, 19867–19872.
27 L. Pan, J. J. Zou, S. Wang, X. Y. Liu, X. Zheng and L. Wang, *ACS Appl. Mater. Interfaces*, 2012, **4**, 1650–1655.
28 J. S. Lee, Y.-J. Lee, E. L. Tae, Y. S. Park and K. B. Yoon, *Science*, 2003, **301**, 818–821.
29 T. C. T. Pham, H. S. Kim and K. B. Yoon, *Angew. Chem., Int. Ed.*, 2013, **52**, 5539–5543.
30 E. S. Kim, N. Nishimura, G. Magesh, J. Y. Kim, J. W. Jang, H. Jun, J. Kubota, K. Domen and J. S. Lee, *J. Am. Chem. Soc.*, 2013, **135**, 5375–5383.
31 M. Lazzeri, A. Vittadini and A. Selloni, *Phys. Rev. B: Condens. Matter Mater. Phys.*, 2001, **63**, 155401.
32 C. H. Kuo, Y. C. Yang, S. Gwo and M. H. Huang, *J. Am. Chem. Soc.*, 2011, **133**, 1052–1057.
33 E. Barsoukov and J. R. Macdonald, *Impedance Spectroscopy*, Wiley & Sons, Inc., Hoboken, New Jersey, 2005.
34 P. S. Archana, R. Jose, C. Vijila and S. Ramakrishna, *J. Phys. Chem. C*, 2009, **113**, 21538–21542.